

In-Cylinder Temperature Estimation from an Optical Spray-Guided DISI Engine with Color-Ratio Pyrometry (CRP)

Hongrui Ma, Robert Stevens, and Richard Stone
Department of Engineering Science, University of Oxford

Copyright © 2005 SAE International

ABSTRACT

Color-ratio pyrometry (CRP) is a technique for estimating the temperature and loading of soot, based on its thermal emission spectrum. This technique is contrasted with conventional two-color pyrometry which requires absolute measurements of the radiation intensity, either at two specific wavelengths or ranges of wavelengths. CRP uses two ratios, obtained by measuring the radiation intensity for three wavelengths or wavelength bands. CRP has been implemented here by using a digital CCD camera, and full details of the calibration are reported. Because of uncertainties in the emissivity of reference sources (such as tungsten ribbon lamps, in which the emissivity depends on temperature and wavelength), then a spectroscopic calibration of the CCD camera has been used. Use of a CCD camera is not straightforward because of internal digital signal processing (DSP), so full details are given of the calibration and technique implementation. Calibration results, together with an error analysis, showed an accuracy of $\pm 50\text{K}$ within the combustion temperature range and a preference for the temperature estimates based on the red/green ratio over the red/blue ratio at low temperatures and the red/blue ratio over the red/green ratio at high temperatures. Temperature estimates are shown to be insensitive to the concentration of soot.

Combustion imaging was later carried out on a spray-guided direction injection spark ignition engine with optical access. Temperature estimates under various imaging timings and mixture strengths are presented. With a fixed operating point the maximum in-cylinder temperature occurred just after top center, and this coincided with the maximum rate of heat release. When the mixture strength was varied, the maximum temperature (at a particular crank angle) was rich of stoichiometric. Finally, temperature and KL results using the variable KL algorithm were reported together with discussions about soot formation.

INTRODUCTION

Direct injection spark ignition (DISI) engines have been widely studied for their combined potential of better

specific power, fuel economy and engine-level emissions. Spray-guided combustion systems are seen to be desirable for the next generation of DISI engines [1-3]. This concept directs the fuel spray straight to the spark plug. Normally based on a narrow spacing configuration, the mixture preparation and combustion do not rely as much on charge motion or piston design as they do on injector characteristics. The appropriate AFR at different engine loads is mainly determined by the spray dynamics. A short mixture formation time until ignition is available due to this narrow spacing, and the engine requires late injection to maintain desirable stratification. Furthermore, liquid spray impingement onto surfaces as well as locally over-rich mixtures can lead to soot and deposit accumulation, rendering the understanding of soot formation, a critical aspect in spray-guided DI systems. It is anticipated that the EURO 5 legislation will include limits on the particulate emissions of gasoline fuelled vehicles, and it is already known that particulate emissions from GDI engines are higher than those from port fuel injection engines.

CCD imaging and color pyrometry are among the most commonly used techniques for characterizing flames and combustion [4] [5]. Color pyrometry relates the temperature of glowing soot and the intensity of the thermal radiation it emits. In conventional two-color pyrometry, for example [6], the light sensing device is calibrated against a black body to determine the apparent temperatures at two specific wavelengths. The emissivity of the soot can be modeled by the widely used empirical correlation of Hottel and Broughton [7]

$$\varepsilon_{\lambda} = 1 - e^{-KL/\lambda^{\alpha}} \quad (1)$$

where λ is the wavelength and KL represents the soot concentration over the optical path length L ; α is 1.39 in the visible range.

The flame temperature can be determined from the ratio of the light intensities at two wavelengths by eliminating an unknown coefficient in the extended Planck's radiation law. Substitution of the flame temperature into equations involving the absolute intensities yields an estimate of the KL factor, which is proportional to the

soot concentration. However, the necessity to have an absolute calibration of the light-sensing apparatus for the two color method makes the result sensitive to factors that alter the visible intensity, such as deposits on optical surfaces or wall reflections/glare.

In contrast, the color-ratio pyrometry (CRP) technique [8][9] uses the ratios of 3 colors to give two independent measures for determining the temperature and KL . The conventional approach normally uses narrow band filters and two light sensors/cameras with beam splitting optics, but it is also possible to use a single color CCD camera [10] to avoid complexities such as the optical setup and image registration.

The advantage of CRP, that absolute intensities are not required, means that it is insensitive to the multitude of problems associated with quantitative intensity measurement. Such problems include calibration errors, variations in optical path and window fouling. Ratio measurements mean that the technique is more rapidly and robustly applicable to engine environments.

The work reported here employs a color CCD camera with three channels (RGB) and uses the ratios of the pixel intensities. The three channels can be reduced to two ratios between red and green (R/G), and red and blue (R/B). In so doing the absolute intensity response is not used and an absolute temperature calibration is not needed. Instead, look-up tables of R/G and R/B ratios are created for the appropriate range of temperature and KL values.

Soot pyrometry estimates directly the temperature of the soot, but due to the almost instantaneous attainment of thermal equilibrium (in 10^{-6} - 10^{-5} s), it can be assumed that the measurement of the soot temperature also represents the burnt gas temperature, i.e. the temperature of the surrounding gas.

Before describing the current work in detail, it will be useful to review some of the practical problems associated with pyrometry. The ideal form of calibration is with a black body, but it is difficult to operate such objects at combustion temperatures. The usual approach is to use a tungsten ribbon lamp, but the emissivity of the filament is a function of wavelength, temperature, age, surface finish and temperature-history of the lamp; consequently there are wide variations in the published data [11]. This issue is side-stepped as it is common for the tungsten ribbon lamp only to have a calibration in terms of an apparent (equivalent black body) temperature at a particular wavelength. This can be one of the wavelengths used in traditional two-color pyrometry (if it does not coincide with a wavelength that is characteristic of chemiluminescence), but there is still the issue of obtaining an absolute calibration at a second wavelength. If absolute measurements are being used, then strictly speaking an *in situ* calibration is needed. One approach is to install a calibrated source in the engine, or a tungsten ribbon lamp can be placed in an equivalent optical path [12].

It must also be remembered that the measurement is not from a single plane, but it is an integration along the optical path. Murphy and Shaddix [13] conclude that the stratification of temperature along an optical path biases temperature measurements towards the higher temperatures along the path, and that the concentration of the hottest soot will bias the KL value. This work suggests that when there is a variation in temperature of 600K with a mean temperature of 1500K, then errors in the measured temperature can readily exceed 100K. There is also the issue of how to model the emissivity of the soot, and this is discussed in detail by di Stasio and Massoli [14]. However, it would appear that this source of error is much less significant than the effect of variations in temperature or KL along the optical path being measured.

With all of these possible sources of error, then why is soot pyrometry a popular technique? It is comparatively cheap and easy to implement, and can be used to give a 2-D plot of the temperature and KL . This is very useful for comparisons between, for example, different fuels or different injection systems.

Color-ratio Pyrometry has not been extensively applied in the literature; therefore this paper describes a generic approach to calibrating a CCD camera for use with CRP. The validation of our calibration method and the temperature prediction with bench tests is also given here. Finally, the color-ratio technique has been applied to an optical access DISI engine with a spray-guided combustion system. Results from measurements over a range of engine operating conditions are reported.

COLOR-RATIO PYROMETRY (CRP)

IMPLEMENTATION

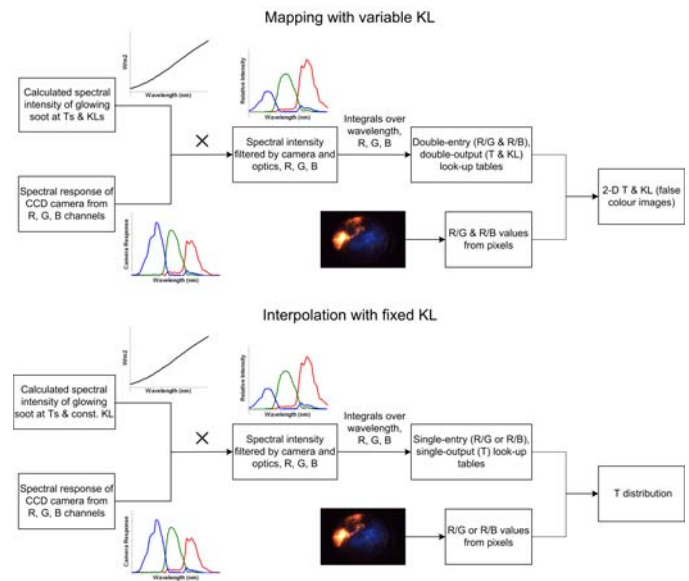


Fig. 1 Procedures for the two strategies in CRP

Two strategies for CRP can be implemented, namely interpolation with a fixed value of KL and mapping with a

variable KL . The schematics of these procedures are shown in **Fig. 1**.

By means of integrals over the full wavelength range, the color-ratio technique is less sensitive to the wavelength selections and emissivity variation usually faced in classical two-color pyrometry. In addition, because the solutions are derived from pre-created look-up tables via interpolation rather than iteratively solving non-linear equations, less computational time is required and the processing is significantly simplified.

When the mapping with a variable KL strategy is applied, both the R/G and R/B ratio values from the image are used and the mapping for temperature and KL is performed to minimize the following characteristic function:

$$E = \left[(R/G)_{T,KL} - \alpha_{i,j} \right]^2 + \left[(R/B)_{T,KL} - \beta_{i,j} \right]^2 \quad (2)$$

where $(R/G)_{T,KL}$, $(R/B)_{T,KL}$ are the inputs from a particular pixel and $\alpha_{i,j}$, $\beta_{i,j}$ are the entries in the look-up tables.

It is worth noting that the blue green (B/G) ratio is not mathematically independent of the R/G and R/B ratios. Additionally, because of decreasing light intensity toward the blue end of the emission spectrum, the B/G is the most susceptible of the three ratios to noise and digitization error. For these reasons the B/G ratio has not been used. Despite the potential of spatially resolving both temperature and KL , previous work [8][10] has shown that the KL solution from the soot pyrometry is often ill-conditioned in some cases, because:

- for a given pair of color ratios there can be multiple solutions of temperature and KL which all map closely to the measured color ratios;
- Uncertainties due to noise in the blue channel of a conventional CCD are high compared with the precision required to determine KL accurately;
- KL tends to be dominated by the environment closest to the detector.

The variation of emissivity with wavelength at different KL s [7] is shown in **Fig. 2**. Assuming a constant KL eliminates the complication of accounting for soot emissivity at the expense of not being able to detect soot concentration.

Fig. 3 shows the R/G and R/B ratios in the look-up tables created with the interpolation method, assuming a constant KL of 0.5.

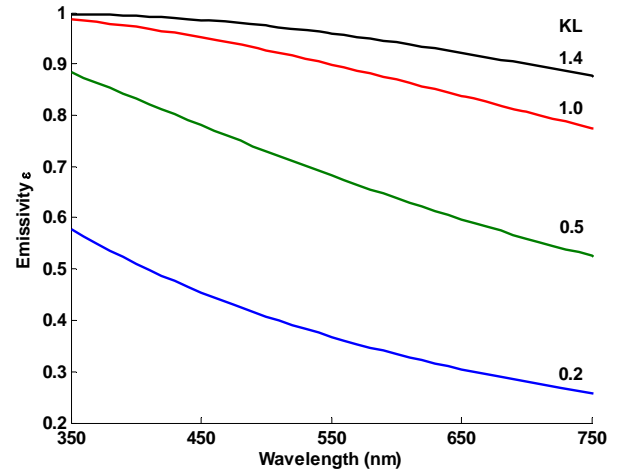


Fig. 2 Variation of soot emissivity with wavelength and KL [7]

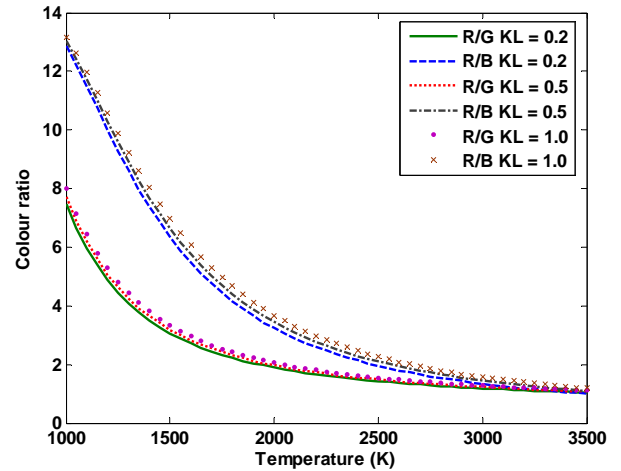


Fig. 3 Expected R/G and R/B ratios of CCD camera response with different KL values

CCD CAMERA CALIBRATION

Experimental setup

Since the soot and tungsten filaments do not have the same emissivity, then a direct calibration is not possible. If the soot was assumed to be a gray body (with constant emissivity), then a black body could be used if one was available at a high enough temperature, however these are difficult to manufacture. Instead it is necessary to determine the spectral calibration of the CCD camera, so as to obtain the camera's color spectral response. This response (which is seen later in **Fig. 10**) is a measure of the camera's sensitivity to different wavelengths for the three color channels (red, green and blue), and is needed for the CRP. The technical specifications for the Pulnix TMC-9700 video camera used in this work can be found in [9].

The calibration was achieved by shining light at different wavelengths onto the camera's CCD sensors. Then the

digital outputs of each of the three channels were extracted from the images using the image processing functions in MATLAB. Fig. 4 shows the setup that was used for the calibration.

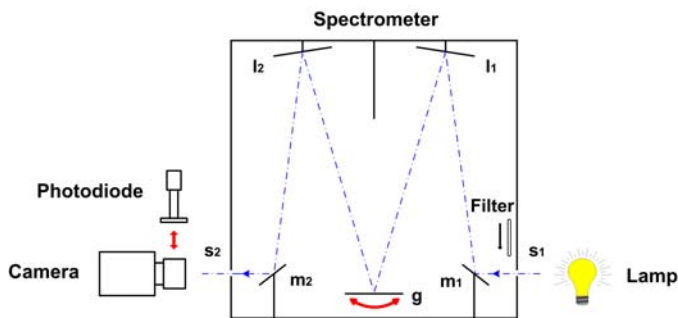


Fig. 4 CCD camera calibration setup

Light from a tungsten lamp (13.5V 5A) was led through the spectrometer (HILGER & WATTS). It was focused onto grating g (1200 lines/mm, blazed @300nm) and then focused onto the camera CCD chip (no objective lens) or photodiode. Both slits s_1 and s_2 were set to 2 mm, giving an output bandwidth of 8 nm. To calibrate the emission spectrum of the lamp and the efficiency of the spectrometer, a photodiode of known spectral sensitivity (ThorLabs DET210) was used to measure the relative intensities when extracting the spectral response curves.

To avoid saturation of images at certain wavelengths, yet make full use of the dynamic range of the camera, different shutter speeds were used.

The spectrometer could potentially introduce the following sources of error:

- Because the bulb emitted much less radiation in the blue range than red, light scatter of the red constituents could bias the measurements in the blue range;
- The second order diffraction effect of the grating could cause some blue radiation (300-400 nm) to appear in the signal in the red range (600-800 nm).

To attenuate these sources of noise, four filters were selected and put behind slit s_1 according to the wavelength range being measured. When the Blue filter was used, most of the radiation above 500 nm would have been heavily attenuated, likewise for the LEE 026 filter, hence eliminating the cross talk between wavelength ranges. The transmission characteristics of these filters were obtained from a spectrophotometer (Perkin-Elmer Lambda 9, usable range 185-3200nm) and are shown in Fig. 5. Also presented in Fig. 5 are three other filters used when testing the linearity of the camera's response with sensitivity and exposure (detailed in the subsequent section).

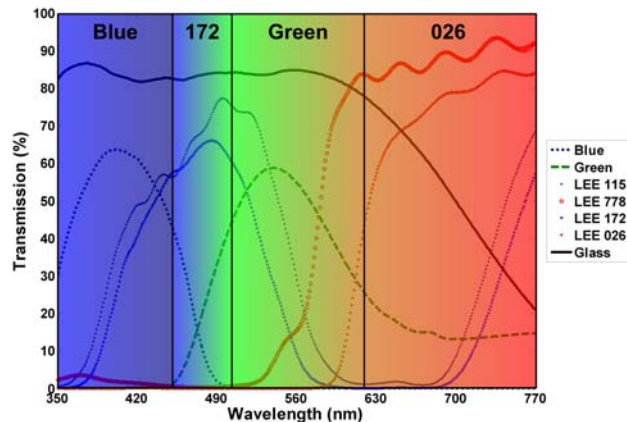


Fig. 5 Transmission characteristics of filters

To obtain a sufficiently detailed and full calibration curve, the wavelength range of 350-770nm (in steps of 10nm) was chosen and 100 images at each wavelength were taken. Images of the background (with the lamp on and slit s_1 closed) were taken as well for noise subtraction.

General image processing

The Pulnix TMC-9700 camera is a one-chip CCD camera with a color filter array (CFA) to provide artificial color information. The staggered pattern of the CFA is shown in Fig. 6.

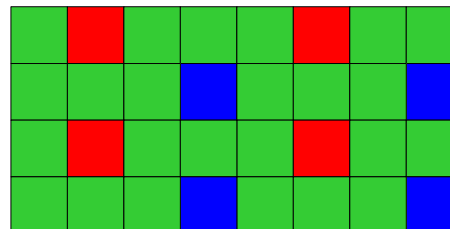


Fig. 6 Color filter array (CFA) of the camera

With the CFA present, each pixel only detects the intensity of a part of the whole radiation wavelength range, and the corresponding color is referred to as its true color. As the camera outputs RGB values for every pixel, then values of the other two color channels are derived from on-chip digital signal processing (DSP). This can introduce cross talk between the true-color channel and the other artificial-color ones depending on the algorithm that has been implemented to provide the color reproduction (whether in RGB or HSV). This effect was seen in preliminary work and led to a systematic error in the CRP. Unfortunately, this DSP process is performed before any image is downloaded into the computer and hence cannot be accessed and corrected for by the user. The same is true for most commercial color cameras, and it should be noted that they may have different CFAs, (the most widely used of which is the Bayer pattern [15]). Other on-chip DSP processes can be optionally performed via the camera software including contrast enhancement, edge sharpening and

white balance correction, all of which are likely to bias the genuine information in the raw images by introducing artifacts. To minimize the cross talk, raw images from the camera were first processed as following:

- only the true color channel for each pixel was kept and the other two color channels were discarded,
- the pixel values of the other two color channels were reproduced through color demosaicing.

Bilinear interpolation [15], modified for the particular CFA of this camera, was selected as the demosaicing algorithm for two reasons:

- it is straightforward to implement and requires little computational resource;
- interpolation of the artificial color pixel is only realized within the color channel, e.g. to derive the red value for a true green pixel only its neighboring true red pixels are involved hence avoiding inter-channel cross talk.

The bilinear color interpolation was implemented differently for the green channel and the red channel while in the same way for the red and blue channels. The interpolation of green value for true red/blue pixels was derived by linear combination of the eight neighboring true green pixels. Take a true red pixel for example:

$$G_{i,j}^R = 0.16 \cdot (G_{i,j-1}^G + G_{i,j+1}^G) + 0.14 \cdot (G_{i-1,j}^G + G_{i+1,j}^G) + 0.1 \cdot (G_{i-1,j-1}^G + G_{i+1,j-1}^G + G_{i-1,j+1}^G + G_{i+1,j+1}^G) \quad (3)$$

where the superscript denotes the true color of that pixel, and i and j mean the pixel lies in the i^{th} row and j^{th} column. The coefficients 0.16, 0.14 and 0.1 were derived so that the two closest (in the same row as $R_{i,j}^R$) pixels were weighted more than the two less close ones (in the same column as $R_{i,j}^R$) and the four furthest ones (on the corner of the 3 by 3 region) were weighted the least. This is because the camera CCD sensor is not a perfect square but a rectangle with an aspect ratio of 1.17 and hence a diagonal-to-side ratio of ~ 1.5 . The green value for a true blue pixel was derived in the same way.

The interpolation of the red value for true green pixels was calculated in two steps. Those true green pixels which have two neighbouring true red pixels above and underneath them were processed first as following:

$$R_{i,j}^G = 0.5 \cdot (R_{i-1,j}^R + R_{i+1,j}^R) \quad (4)$$

Then for the rest undetermined non-true red pixels (of which there are three in a row between two pixels with known red values), linear interpolation was applied. The interpolation of blue value for true green pixels was carried out in the same way.

The thermal radiation from glowing tungsten or soot at a temperature lower than 3000K is red-dominant whilst the radiation from chemiluminescence is blue-dominant, so pixel saturation is more likely to happen on the red and blue channels than the green one. When pixel saturation occurs on a red or blue channel, pixels within the 3 by 7 array, the center of which is the saturated red or blue pixel, will be biased by the saturated pixel in the demosaicing process. Therefore, such pixels are assigned 255 at the end of the demosaicing code so that they can be readily excluded at a later stage.

It should be noted that when CRP is applied, although the camera is a single-chip one, a flat field correction must be carried out for the three color channels separately, i.e. three flat field matrices, otherwise any correction coefficient would be cancelled out when a ratio is generated; to some extent, the flat field correction for the color-ratio technique is similar to a weak white balance correction.

Camera response test

The camera's sensitivity was tested on the same spectrometer setup with the following approach: images were captured at a series of wavelengths; at each wavelength, a particular shutter setting was first selected without any filter to best utilize the dynamic range. Then different combinations of the seven filters (**Fig. 5**) were chosen to reduce the level of radiation into s_1 , whilst maintaining the shutter setting for that wavelength. Such images were normalized to the camera's response in the 100% transmission case (no filter). Results regarding the camera's response linearity with sensitivity are shown in **Fig. 7**. The responses from the three color channels are plotted separately. The non-linearity was within 2% over the wavelength range of interest, and given the 1-2% shot-to-shot noise level, the camera's response sensitivity was taken to be linear.

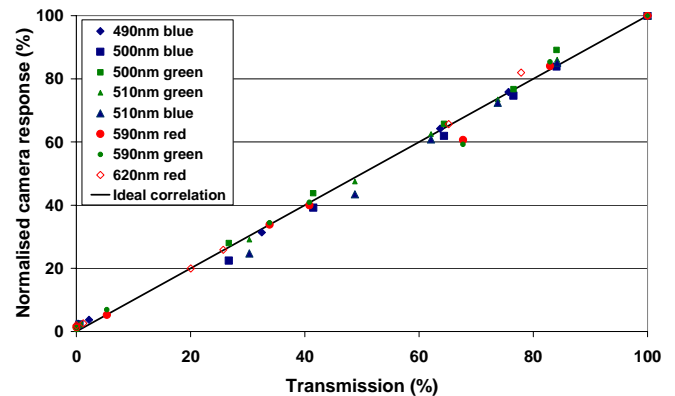


Fig. 7 The camera's response test for linearity with sensitivity

The linearity of the camera's response with exposure duration was also tested using the same spectrometer setup, so that:

- images were captured at a series of wavelengths;
- at each wavelength, an optimal shutter setting was first selected without any filter,
- then different combinations of the seven filters were chosen to approximately give an each-step-halved transmission so that a doubled exposure time could be used to maintain the camera's response.

Since the camera's sensitivity was proved to be linear, the exposure-response correlation could be described by:

$$R_{i,j} = \frac{I_i}{I_j \cdot \gamma_{\text{tran}}} \quad (5)$$

where: $R_{i,j}$ is the response ratio between two shutter settings i and j , I_i and I_j represent measured camera responses with shutter settings i and j , and γ_{tran} is the transmission data involved.

Fig. 8 presents the camera's response to the exposure duration. The shutter effect was then taken account of by normalizing the spectral calibration images captured using different shutter settings with respect to exposure time.

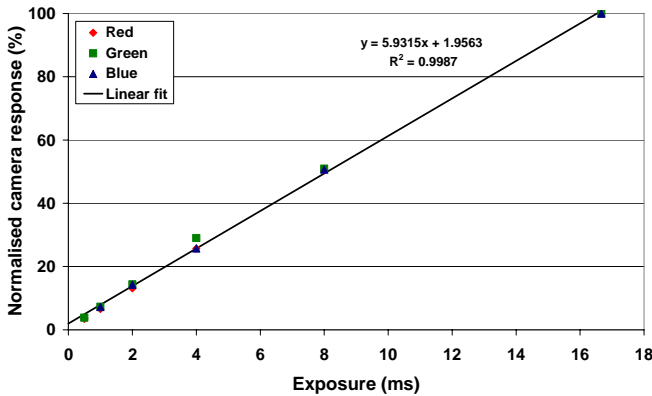


Fig. 8 The camera's response test for linearity with exposure

Calibration image processing

The diffracted light beam showed an elliptic geometry and its intensity varied across the two dimensions of the image. Therefore only the central part (60 by 50 pixels) of each image was extracted and processed; this effectively reduced the bandwidth of the wavelength analyzed to ~1nm.

Because the photodiode has a non-linear sensitivity with respect to wavelength, experiments with lasers of various wavelengths were conducted. **Fig. 9** (top) gave the sensitivity of the photodiode with respect to wavelength. The polynomial fit to these measured points showed good agreement with the datasheet supplied by

the manufacturer (the outliers are due to uncertainties and instabilities in laser energy), and hence the manufacturer's calibration was employed in the following steps. This, together with the digital voltmeter (DVM) reading from the photodiode indicated the spectral emission of the tungsten lamp at a particular temperature (**Fig. 9** (bottom)). The DVM readings were taken when the photodiode detected the bulb radiation through the various filters and hence displayed a multi-stage shape. The 'corrected response' refers to the photodiode response after the photo-diode sensitivity normalization.

To correct for the intensity variation of the tungsten lamp with wavelength, the RGB components at wavelength λ were normalized to the maximum intensity I_{max} by multiplying the factor $I_{\text{max}}/I_{\lambda}$, where I_{λ} was the intensity at wavelength λ from **Fig. 9** (bottom). The final spectral response of the camera is shown in **Fig. 10**.

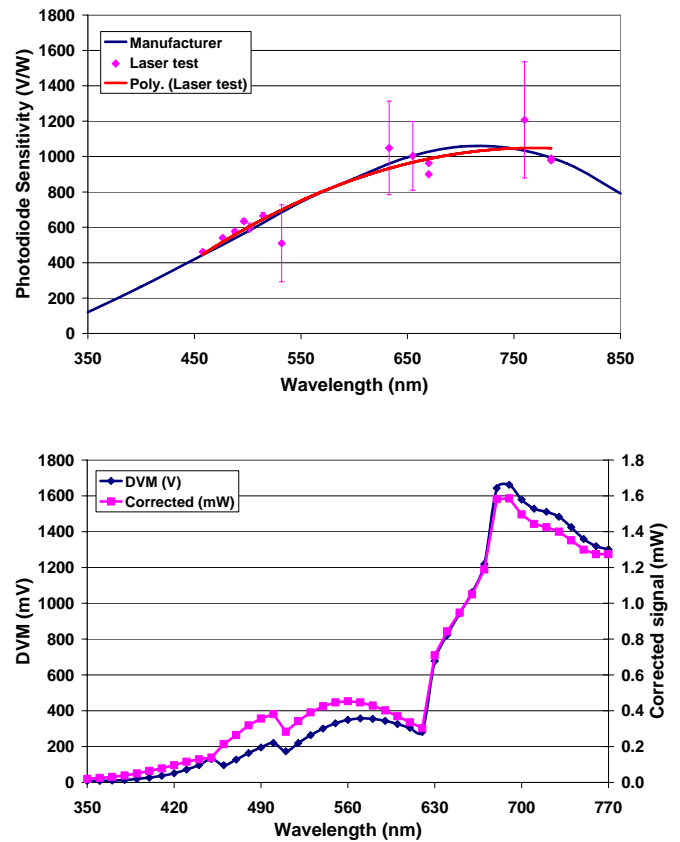


Fig. 9 Photodiode sensitivity (top) and signal from the tungsten bulb (bottom) with respect to wavelength

As seen in **Fig. 10**, in the range of green (500-600nm) the spectral responses of red and blue follow each other. This suggests that the signal from the green channel has affected the red and green channels. One possible cause of this cross talk is miss-registration or misalignment between the CCD chip and the CFA, that is, signal that falls onto the true-green pixels spreads to the adjacent R or B pixels. As there will be variations

between cameras and the published data is only nominal, it is essential to calibrate each camera.

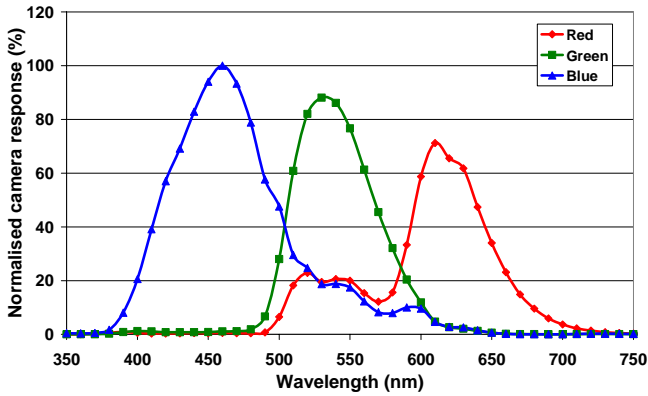


Fig. 10 Normalized spectral response of the camera

The sensitivity of the system could be enhanced by using a filter that would attenuate the longer wavelengths, so that at a mid-range temperature each of the 3 color channels would have the same signal level.

VALIDATION OF CRP

To verify the CRP using the calibrated spectral response of the CCD camera, three sets of experiments were conducted, namely: imaging of a blackbody cavity, a tungsten filament lamp and a tungsten ribbon lamp. A 50mm lens with variable aperture was used for focusing. As only ratios were dealt with in the analysis, the non-linear effect of the aperture setting would not need to be corrected for. The transmission characteristics of the lens and optical pathway were also measured with the spectrophotometer and accounted for in the subsequent analysis.

Black body imaging

The black body used in this experiment was made from a steel bar with a cavity in one end, the diameter of which was an order of magnitude smaller than the length of the tube. The camera was focused to the inside back of the black body through the hole. An aluminum tube was manufactured to cover the camera lens to prevent inclusion of extraneous light. The black body (with a radiation shield) was then heated up by an oxy-acetylene flame, and its temperature was recorded by a thermocouple inserted behind the cavity in the black body.



Fig. 11 Sample images from the validation experiments: black body (left), tungsten filament lamp (middle), and tungsten ribbon lamp (right)

Temperature readings and images of the black body were taken continuously until the solid end of the black body melted. **Fig. 11** (left) is a typical image of the black body from the experiment.

Comparisons between the measured and inferred temperatures of the black body are shown in **Fig. 12** together with the corresponding standard deviations. The correlation between results from the R/G ratio and the measured temperatures was better and more linear than that from the R/B ratio. This is because in such a low temperature range the black body would emit much less blue constituents than red and green. Furthermore, the camera's dynamic range is only 8 bit. Therefore, it is difficult to resolve the temperature from the R/B ratio and such results would be associated with large uncertainties. This is also reflected by the standard deviation results. Better precision could be achieved with a 10 or 12-bit camera.

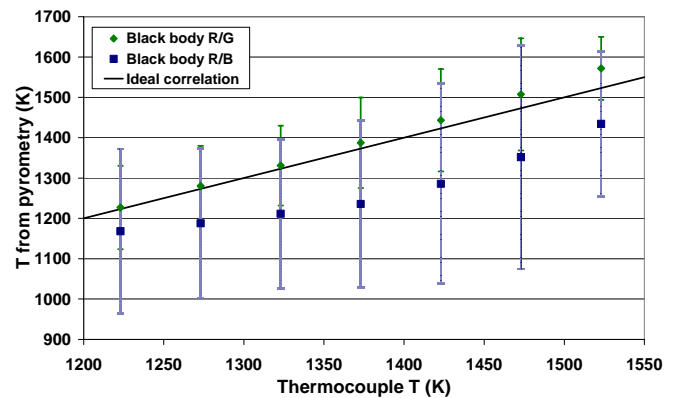


Fig. 12 Correlation between measured and inferred temperatures of the black body

Tungsten filament imaging

The same tungsten lamp used in the camera spectral calibration process was utilized in this experiment. **Fig. 11** (Middle) is a typical image of the filament from the experiment. Instead of running the lamp under nominal conditions, the voltage and current on the lamp were varied to give different intensities and distributions of light, and the voltage and current were recorded to estimate the filament's resistance as a separate temperature indicator. Temperatures from the CRP were then compared with the ones derived from the measured filament resistance [16]. The same necessary steps of image processing as above were carried out.

Initially the lamp filament was assumed to be a grey body (constant emissivity). Measured emissivity data for tungsten ribbon lamps at different temperatures and wavelengths [11] were then used subsequently for improved accuracy. The emissivity data used are plotted in **Fig. 13**, but it must be remembered that there are wide variations among the published data.

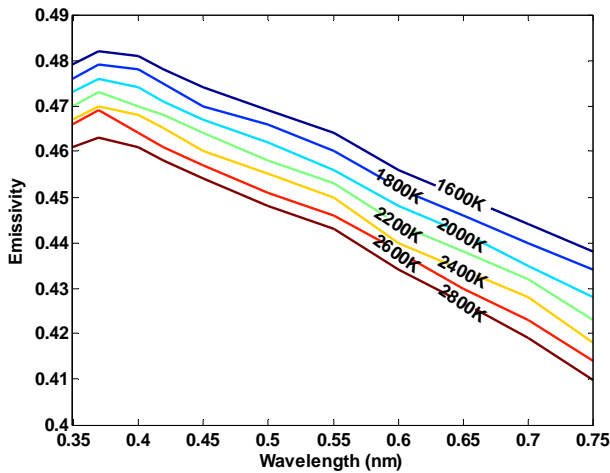


Fig. 13 Tungsten emissivity data used in the tungsten filament test, data selected from [11]

Fig. 14 shows the correlation between temperatures predicted by CRP and filament resistance together with the corresponding coefficient of variation (CoV) for both cases. The CoV presented here was defined as the average of the spatial CoV of each image from the image sequence (100 images under the same condition), hence reflecting the temperature variation across the selected part of the filament.

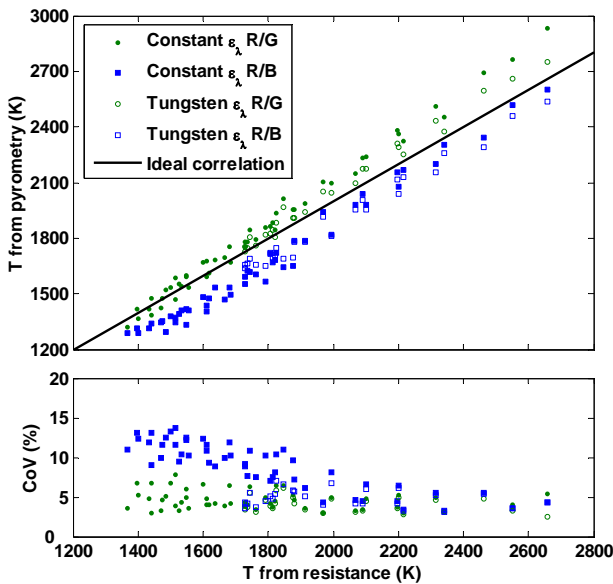


Fig. 14 Relation between temperatures estimated with CRP and filament resistance

With realistic emissivity data the R/G ratio-based temperatures were generally < 100K lower than the ones with the grey body assumptions when the resistance indicated temperatures were below 2400K. This is because the emissivity of tungsten decreases with increasing wavelength and the relative proportion of long-wavelength radiation to short-wavelength radiation was smaller than that in the constant emissivity case. So

the calculated color ratios in the look-up tables become smaller, and for a given R/G ratio of a pixel, the estimated temperature moves towards the lower values. This effect is not so distinct for results based on the R/B ratio; the R/B data points with realistic emissivity values became lower than the ones with constant emissivity at around 2000K resistance temperature and above. Again this is because the lamp did not emit as much blue light as green and red at low temperatures and larger uncertainties were likely to be introduced. However, the difference introduced by using experimental emissivity is insignificant within the temperature range for engine combustion. Moreover, the database of measured emissivity is coarse, incomplete, strongly dependant on the surface condition and, to a large extent, self-inconsistent for the wavelength range of interest here [11]. In conclusion, the temperature calibration against a tungsten filament should not be treated as an absolute reference because of uncertainties in the emissivity and uncertainty in the temperature deduced from the filament resistance.

In summary, the temperatures derived from the resistance of the filament agreed with the ones from the color-ratio method better for R/G ratios at low temperatures (< 2200K) and better for R/B ratios at high temperatures (> 2200K). Again, temperatures derived from the R/B ratios are better resolved at high temperatures, indicating the potential of using R/B results as a supplement for checking the R/G results in the high temperature range.

The discrepancies from the unity line in **Fig. 14** may partly be due to uncertainties in the inference of the temperature from resistance, e.g. the non-uniform temperature distribution across the filament, the different resistance-temperature behavior of other parts of the lamp etc.

The overall CoVs of this experiment scatter within 3-7% in the range of 1600-2600K except those low-temperature R/B points with constant emissivity.

Tungsten ribbon imaging

A high-stability tungsten ribbon lamp (POLARON 10/V) was employed for its capability of calibrating temperature measuring devices. A typical image of the ribbon lamp from the experiment is shown in **Fig. 11** (right).

The lamp was calibrated in terms of radiance temperature by reference to a National Physics Laboratory (NPL) standard tungsten ribbon lamp which has been calibrated using a precision radiation thermometer, which had itself been calibrated with reference to a blackbody source at the freezing point of gold (~1064 °C). At each calibration current the radiance temperature of the test lamp is determined by comparison with the calibrated standard lamp using a comparator.

The radiance temperature corresponds to the temperature of a black body at the calibration wavelength (660nm for this lamp). The radiance temperature is not the true ribbon temperature, but the temperature that a black body would have to be at, in order to emit the same intensity of radiation at the specified wavelength. Therefore, conversion between the archived radiance temperature of the lamp and the actual ribbon operating temperature must be done based on Planck's Radiation law and an estimate of the emissivity

$$I_{\lambda b} = \frac{2C_1}{\lambda^5 (e^{C_2/\lambda T_b} - 1)} \quad (6)$$

where: $I_{\lambda b}$ is the spectral intensity emitted by a black body, C_1 and C_2 are known as Planck's radiation constants, having values of $1.871 \cdot 10^{-16} \text{W} \cdot \text{m}^2$ and $1.439 \cdot 10^{-2} \text{m} \cdot \text{K}$ respectively.

Real objects such as tungsten are not black-body emitters, and radiate less energy at each wavelength than the equivalent black body value. With the spectral emissivity of tungsten ϵ_λ present, Eq. (6) becomes:

$$I_{\lambda t} = \epsilon_\lambda I_{\lambda b}(\lambda, T_b) = \epsilon_\lambda \frac{2C_1}{\lambda^5 (e^{C_2/\lambda T_t} - 1)} \quad (7)$$

Letting $I_{\lambda t}$ equal $I_{\lambda b}$ and substituting Eq. (6) into Eq. (7), the correlation between the temperature of the tungsten ribbon T_t and its corresponding blackbody temperature T_b (also the radiance temperature) can be written as:

$$T_t = \frac{C_2}{\lambda_c \ln(\epsilon_\lambda e^{C_2/\lambda T_b} + 1 - \epsilon_\lambda)} \quad (8)$$

As shown in **Fig. 15**, a fairly linear correlation existed between the estimated temperatures with CRP and the deduced lamp operating temperatures, it being more linear for the R/G results than the R/B results. The R/B points seemed to match with the lamp operating temperature better than the R/G ones, however, they were more scattered and the difference between the two series decreased with increasing lamp temperature. Again there is uncertainty in the emissivity of the tungsten ribbon. This manifests itself as uncertainty in its true temperature and as uncertainty in the spectral intensity of the radiation so the ribbon lamp does not provide an absolute reference.

An examination of the spectral output of the tungsten ribbon lamp in the range 640-910nm at each temperature suggests that there might be a systematic error in the blackbody calibration of the lamp temperature; this could be an aging phenomenon. In **Fig. 15** a broken line has been added to account for this deduced temperature offset of 70K.

The overall CoVs of this experiment fall within 3-10% for the temperature range of 1600-2000K except those low-temperature R/B points analysed assuming a constant emissivity.

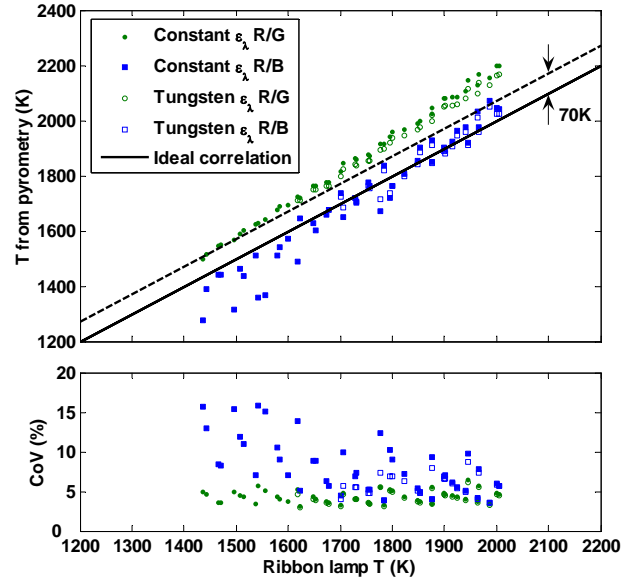


Fig. 15 Relation between the temperature estimated with CRP and the estimate of the ribbon lamp operating temperature

Concluding remarks on the temperature calibration

In comparisons between the temperatures derived from CRP and the reference temperatures provided by the three validation experiments, the R/G color ratio results showed excellent linearity; the R/B results were more scattered but were useful as supplementary information, particularly for the high temperature range – this may be improved using a camera of higher dynamic range.

To minimize the possible error due to all the noise sources and best utilize both the R/G and R/B color ratios, a weighted-mean temperature T_c was adopted as the output from the CRP:

$$\begin{aligned} T_c &= a \cdot T_{R/G} + (1-a) \cdot T_{R/B} \\ a &= 1.5 - T_{R/B} / 2000 \\ |T_{R/G} - T_{R/B}| &< 200\text{K} \end{aligned} \quad (9)$$

where a and $1-a$ are the weighting coefficients with an applicable range of 1000-3000K. A premise of this calibration is that the difference between the temperatures from R/G and R/B estimates must be below 200K. Any image not compliant with this premise is likely to be due to chemiluminescent flames and hence was not taken as valid.

Throughout the range of 1200-2800K, the weighted temperature from the blackbody and tungsten filament

experiments showed a deviation of less than $\pm 50K$ from the ideal correlation and the one from the tungsten ribbon experiment is always 50-100K higher than reference. Taking account of the 70K systematic offset mentioned in the previous section, the deviation in the tungsten ribbon experiment is also less than $\pm 50K$.

Error analysis

Firstly, the ± 1 bit digitisation error caused by the A/D conversion process of the camera was investigated. Such an error in the color values (intensity) can lead to an error in the color ratios, which results in an intrinsic error on the temperature estimate. Quantifying this error helps to understand the accuracy of the color-ratio method and set a reasonable step size in the look-up tables. The digitisation error can occur on any one, two or three color channels at the same time, therefore the worst case, in which there was +1 bit error in the red channel and -1 bit error in the green and blue channel was chosen for this study.

For a range of temperatures, a relative intensity of 127 was assigned to the red component, which was stronger than signals from the other two channels, and the green and blue values were calculated by dividing the red value by the ratios in the look-up tables. Then 1 was added to the red values and subtracted from the green and blue values to generate new color ratios. These new ratios were mapped back using the original look-up tables and the error-added temperatures were returned. The error from the R/G and R/B ratio calculation is presented in **Fig. 16**.

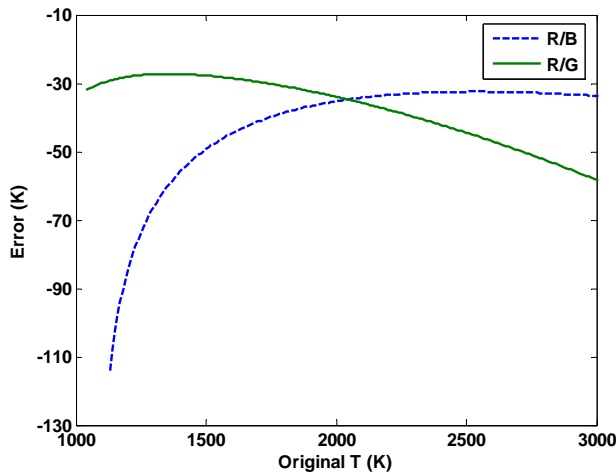


Fig. 16 The effect of a 1 bit digitization error on the estimated temperature

The step size of the look-up tables used for **Fig. 16** was 10K and was found to give reasonable performance. The error presented is always negative because this case referred to +/-1 bit error introduced to the numerator and denominator of the color ratios respectively. The error curves would be approximately inverted for the opposite case.

Since the 1 bit digitisation error may not happen on all three channels at the same time, the case presented here indicates the worst-case error. However, the relative intensity of 127 may not be achieved and the utilisation of the dynamic range may be poor in practice. Taking these two factors into consideration, error in the temperature estimation due to the ± 1 bit digitisation error can be predicted to be within $\pm 50K$ for the temperature range of engine combustion (1500-2600K). It should also be noted that although **Fig. 7** indicates linearity uncertainties of $\sim 2\%$ (2-3 counts for a camera response of 127 counts), the source of such uncertainties are most likely to be a combination of both shot-to-shot noise and digitization error which cannot be decoupled from one another. Therefore, the ± 1 bit digitisation error is still representative of most cases encountered in practice.

The ± 1 bit digitisation error analysis above was applicable to a single pixel, whilst the effect of random noise on a global averaging basis was studied as well since spatial averaging was applied in the validation experiments. In this study, standard artificial images of uniform color ratios were produced according to the look-up tables for a series of temperatures. Then different levels of random noise was added to the three color channels of these images, namely, noise-to-signal ratio (NSR) of 0.05-0.25 in steps of 0.05, in which case signal means the color value of a particular color channel in the images. These new images were processed using the original look-up tables (step size 10K), and the returned error-added temperature field was spatially averaged. **Fig. 17** shows the error from the R/G and R/B ratio calculation.

The resultant error displayed a feature with respect to the original temperature as opposed to a random distribution that one would expect. However, this is a genuine fact in particular for the color-ratio technique presented here. Firstly, the algorithm for CRP was interpolation with fixed KL in which the boundaries of the look-up tables for interpolation had to be set before any calculation was carried out; in this study the boundaries were 1000 and 3000K. Therefore, as the original temperature approached either boundary, the random noise distribution added to the original temperature field was cut off on one side and became distorted, resulting in the increasing deviation from zero on both ends of the x axis in **Fig. 17**. One reason why the error behaved differently at low temperature and high temperature may well be the shape of the color ratio curves in **Fig. 3**, which monotonically decrease with decreasing gradient. For instance, adding the same amount of numerical noise (NSR) to the standard image at 1000K and 3000K would result in a different amount of temperature error due to the different scales of interpolation. By this means, the temperature error can be estimated to be $\pm 50K$ for the temperature range of 1800-2600K using R/G results and 2400-3000K using R/B results.

Recalling the deviation of the experimental results from the 'unity' line in the above sections, this deviation is

likely to be the combined error of the ± 1 bit digitisation error of individual pixels, the spatially averaged random error and the uncertainties in the experiments themselves.

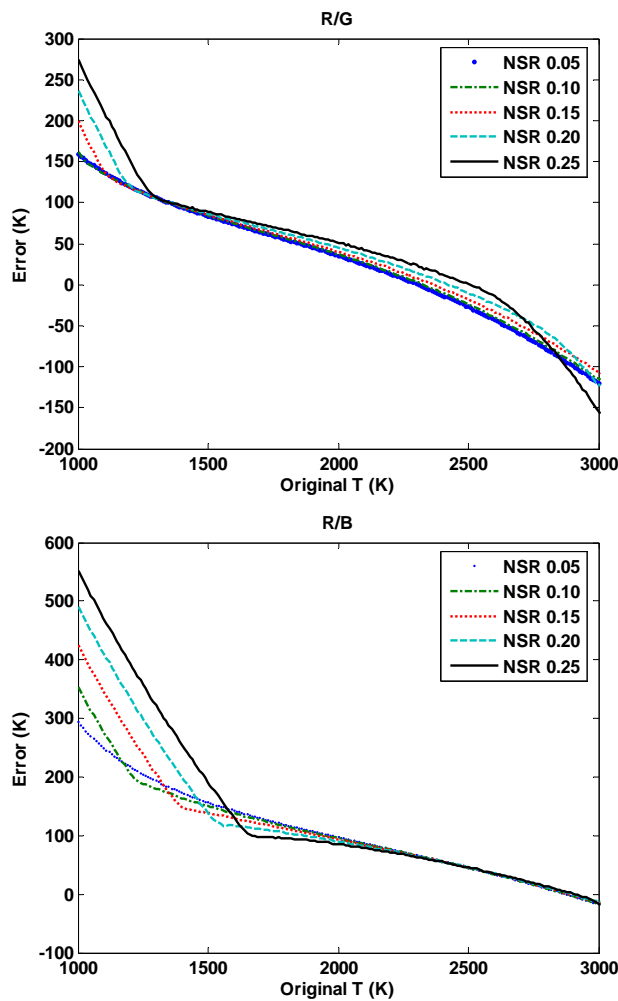


Fig. 17 Effect of random noise and global averaging on temperature estimation

DISI ENGINE RESULTS

OPTICAL RESEARCH ENGINE

The engine was a Jaguar single cylinder research engine with a spray-guided DISI combustion system. Optical access could be achieved in five ways:

- a full quartz cylinder liner
- a short quartz annulus which goes on top of a metal liner
- a similar short aluminum annulus with four side windows
- a flat quartz window (60mm diameter) fixed in the piston crown
- a triangular quartz window embedded in the cylinder head to view the pentroof region of the combustion chamber

A typical arrangement for the pyrometry measurement on this engine is shown in **Fig. 18**. The engine has a bore of 89mm, a stroke of 90mm and a compression ratio of 11.

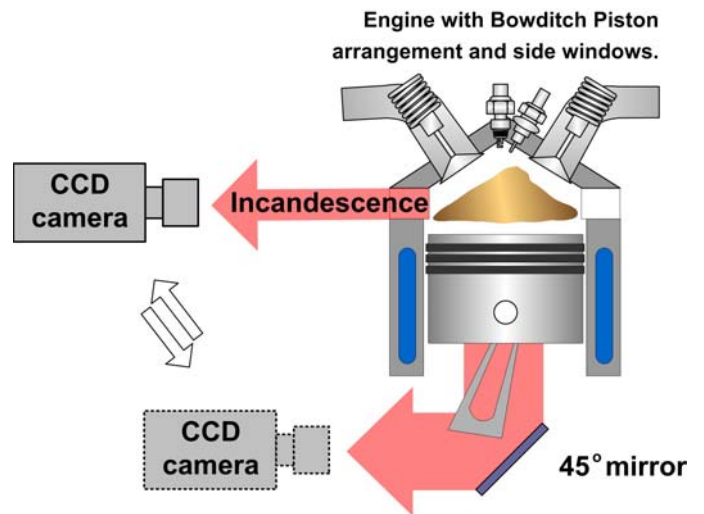


Fig. 18 Set-up for measurements on the optical DISI engine with CRP

CCD IMAGING RESULTS

An image sequence of 100 images was taken for each engine operating condition with an angle increment of 5° after taking 10 images at each crank angle setting. This gave an imaging duration of 50° after ignition. The exposure time was adjusted accordingly to avoid major image saturation but fixed within each image sequence. All image results presented in this section were flat-field corrected and were for engine operating conditions of:

1500RPM, ignition 35° before top dead center (TDC), and injection timing of 280° before TDC.

A sample image from the Pulnix TMC-9700 CCD camera through the pentroof window is shown in **Fig. 19**, with the engine operating in a rich homogeneous mode, with toluene and a lambda value of 0.8.



Fig. 19 Sample image from the engine in homogeneous mode, with toluene, $\lambda = 0.8$, ignition timing 35° before TDC, injection timing 280° before TDC, image timing -10° after TDC

The pyrometry results for this sample image have been analyzed with different methods, and the results are summarized in **Table 1**. With variable KL , both the R/G and R/B color ratios were input to the map created beforehand with temperature limits of 1400-3000K and KL limits of 0.1-1.4 representing typical soot conditions. This resulted in a single temperature output as well as KL .

	Variable	KL			Grey body
		0.2	0.5	1.0	
mean _{R/G}	2397	2502	2550	2601	2649
mean _{R/B}		2422	2471	2523	2572
st.d. _{R/G}	241	271	265	260	255
st.d. _{R/B}		283	277	271	266

Table 1 Summary of pyrometry results for the sample image in **Fig. 19** with different KL settings

The predicted temperature with fixed KL increases with the prescribed KL and was the highest when the grey-body assumption was made. This is because the emissivity decreases with KL , more with a smaller KL , according to Hottel and Broughton's formula (**Fig. 2**) and hence the longer wavelength range was weighted less in the integrating process when a prescribed KL was introduced.

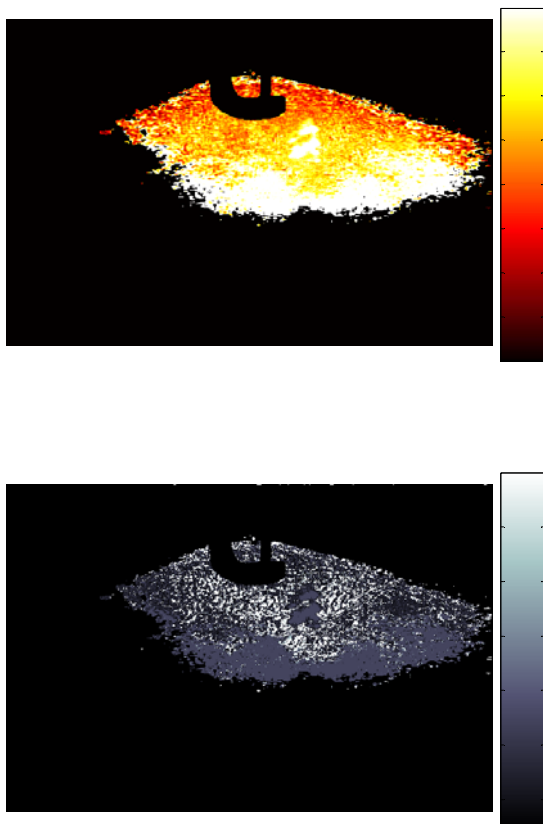


Fig. 20 Temperature (top) and KL (bottom) distribution for the sample image of **Fig. 19** with variable KL

There was a small difference in temperature between the variable KL and fixed KL cases. An unfortunate

corollary of this is that the calculations of KL will be ill-conditioned. The standard deviations of the spatial temperature distribution in all cases are comparable and led to a CoV of ~10%.

Fig. 20 shows the false color images of in-cylinder temperature and KL distribution from the sample image (**Fig. 19**) using the variable KL strategy. Invalid areas such as outside of the pentroof window, the spark plug and the injector tip were overlaid as a black layer. Algorithms were incorporated for detecting saturated pixels and potential chemiluminescence pixels (R/B < threshold). Such pixels are obvious in **Fig. 19** and shown in **Fig. 20** as the higher limit values but not included when the spatial average was calculated.

Fig. 21 presents the results for the spatially averaged temperature T_c and the crank angle timing from the image sequence of $\lambda = 0.8$. The first detectable flame occurred 15° after ignition and the predicted temperature seemed to peak around 10° after TDC. This coincided with the time when ~50% mass fraction burnt and when the maximum heat release rate occurred. Because the intensity of the soot emission varied dramatically over time, the image timing range was limited by the relatively narrow dynamic range of the camera system.

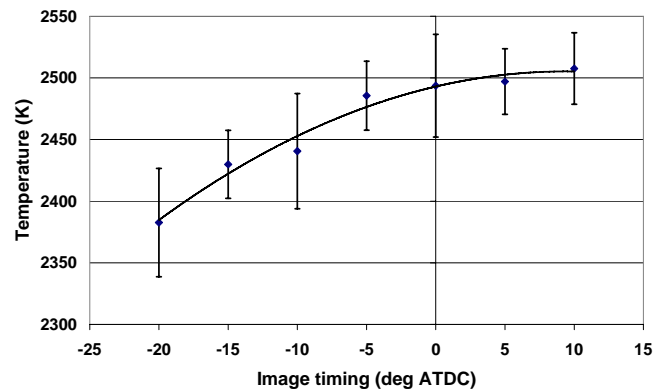


Fig. 21 Relation between temperature from CRP and crank angle with $KL = 0.5$, $\lambda = 0.8$.

The relation between the spatially averaged temperature T_c and the mixture strength is shown in **Fig. 22** with an image timing of 5° after TDC. The data points were sparse and more scattered at lean operations because

- the combustion chemiluminescence became dominant in most of the images which must be excluded from the analysis;
- the engine instabilities increased when operating lean.

Due to the large associated uncertainties, caution is needed when interpreting images from mixtures leaner than stoichiometric with the CRP. However, as would be expected, the polynomial-fit curve shows a temperature peak occurring slightly richer than stoichiometric.

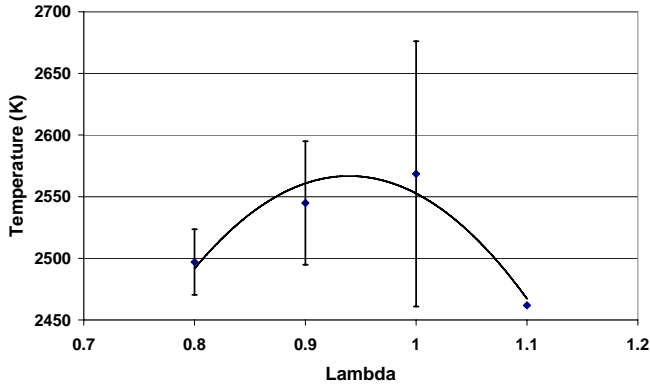


Fig. 22 Relation between temperature from CRP and mixture strength with $KL = 0.5$; image timing = 5° after TDC. Each data point comes from a separate image

Despite the limited KL resolution when adopting the variable KL strategy, a parameter, $N * KL$, can be used to depict the loading of soot:

$$N * KL = \sum_i KL_i \cdot N_{KL_i} \quad (10)$$

where: N stands for the number of pixels, representing the area within which the pixels give a certain KL value.

Any KL value above 1.3 was likely to be a result of image saturation or chemiluminescence, and hence it was excluded from the calculation. Results with variable KL from the same image sets as in **Fig. 21** and **Fig. 22** are shown in **Fig. 23** and **Fig. 24**.

The temperature curve in **Fig. 23** looks largely the same as **Fig. 21**, again indicating that the temperature estimate is insensitive to the concentration of soot. As expected, the loading of soot increased as combustion proceeded and reached the highest level at the latest imaging crank angle.

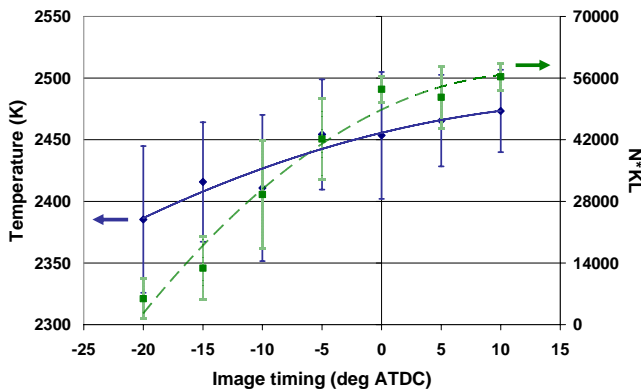


Fig. 23 Relations between variable- KL results from CRP and crank angle, the other conditions the same as in **Fig. 21**.

The relation between $N * KL$ and mixture strength in **Fig. 24** shows that the soot production was the highest at lambda 0.8 and quickly diminished to extremely low levels as the mixture went lean. The significant discrepancies in temperature between **Fig. 22** and **Fig. 24** when the mixture went lean could be because that the variable- KL algorithm is more sensitive to chemiluminescence than the fixed- KL one.

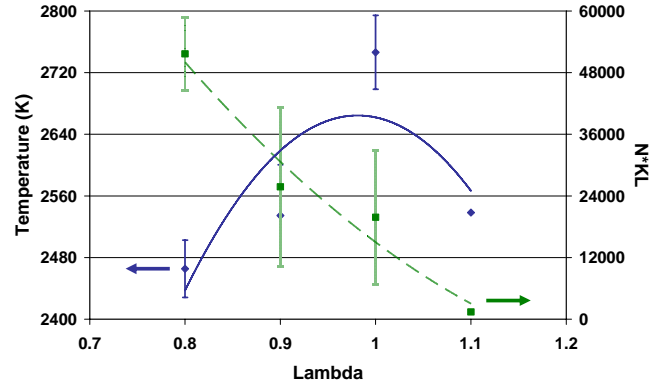


Fig. 24 Relations between variable- KL results from CRP and mixture strength, the other conditions the same as in **Fig. 22**.

CONCLUSIONS

A spectral calibration was carried out to identify the spectral response of a color CCD camera, with which color-ratio pyrometry was applied to images from three validation experiments, namely: imaging of a blackbody cavity, a tungsten filament lamp and a tungsten ribbon lamp. The algorithm and implementation of CRP and the required image processing have been discussed.

Results from the bench experiments showed satisfactory agreement between the temperature derived from CRP and the 'reference' temperature. The sources of uncertainty in the temperature and emissivity of tungsten filaments have been discussed. The R/G results were better at lower temperatures and the R/B results were better at higher temperatures, revealing the potential of an overall temperature calibration for the color-ratio technique to best utilize information obtained from both the R/G and R/B ratios. The deviation of experimental data from linear fitting was within $-50/+100K$ in the temperature range of 1200-3000, hence rendering the CRP a practical technique for estimating in-cylinder temperatures of internal combustion engines.

Error analysis was performed to understand the accuracy of the color-ratio method, including the effect of camera digitisation error and spatial averaging of random noise on the temperature estimation. Taking the worst case of the ± 1 bit digitisation error into consideration, the error in the temperature estimate was still within $\pm 50K$ for the temperature range of engine combustion (1500-2600K). The possible error caused by

spatially averaged random noise was estimated to be within $\pm 50K$ for the temperature range of 1800-2600K.

Combustion images from a spray-guided DISI engine were then interpreted using the CRP. A comparison of results from different prescribed KL values indicated that the predicted temperature was insensitive to the KL setting (whether variable or fixed). The general trend was that the temperature increased with increasing prescribed KL , and reached the highest when the soot was assumed to be a grey body. False color images of spatial temperature and KL distribution have been demonstrated; however, the KL solutions were ill-conditioned. Using a camera with a better dynamic range would help increase the reliability of the KL measurements.

Finally relations between the spatially averaged temperature and the crank angle timing as well as mixture strength have been presented. The camera's dynamic range posed constraints on the selectable range of image timing. Similarly, results with variable KL were reported and the parameter $N * KL$ was introduced to extract information of soot formation. Due to the presence of combustion chemiluminescence, additional care is necessary when dealing with images from lean engine operating conditions.

ACKNOWLEDGMENTS

Support from EPSRC, Jaguar and Shell Global Solutions is gratefully acknowledged. Thanks are also directed to Prof. Hua Zhao at Brunel University for providing the tungsten ribbon lamp facility.

REFERENCES

1. Wirth, M., Zimmermann, D., Friedfeldt, R., Caine, J., Schamel, A. Davies, M., Peirce, G., Storch, A., Ries-Müller, K., Gansert, K.-P., Pilgram, G., Ortmann, R., Würfel, G. and Gerhardt, J. (2004). 'A Cost Optimised Gasoline Spray Guided Direct Injection System for Improved Fuel Economy', Proc IMechE. — Fuel Economy and Engine Downsizing.
2. Georjon, T., Bourguignon, E., Duverger, T., Delhaye, B. and Voisard P. (2000). 'Characteristics of Mixture Formation and Combustion in a Spray-Guided Concept Gasoline Direct Injection Engine: An Experimental and Numerical Approach', SAE Technical Paper, No. 2000-01-0534.
3. Befrui, B., Kneer, R., Breuer, S., Reckers, W., Robart, D., Wanlin, H. and Weiten, C. (2002). 'Investigation of a DISI Fuel Injector for a Close-Arranged Spray-Guided Combustion System', SAE Technical Paper, No. 2002-01-1133.
4. Zhao, H. and Ladommatos, N. (1998). 'Optical Diagnostics for Soot and Temperature Measurement in Diesel Engines', Progress in Energy and Combustion Science, Vol. 24, No. 3, pp. 221-255.
5. Vattulainen, J., Nummela, V., Hernberg, R. and Kytölä, J. (2000). 'A System for Quantitative Imaging Diagnostics and Its Application to Pyrometric In-Cylinder Flame-Temperature Measurements in Large Diesel Engines', Measurement Science and Technology, Vol. 11, No. 2, pp. 103-119.
6. Ahn, S. K., Matsui, Y., Kamimoto, T. and Matsuoka, S. (1981). 'Measurement of flame Temperature Distribution in a D. I. Diesel Engine By Means of Image Analysis of Nega-Color Photographs', SAE Transactions, Vol. 90, SAE Paper 810183, 1981.
7. Hottel, H. C. and Broughton, F. P. (1932). 'Determination of True Temperature and Total Radiation from Luminous Gas Flames', Industrial and Engineering Chemistry: Analytical Edition, Vol. 4, No. 2, pp. 166-175.
8. Simonini, S., Elston, S. J., and Stone, C. R. (2001). 'Soot Temperature and Concentration Measurements from Colour Charge Coupled Device Camera Images Using a Three-Colour Method', Proc IMechE, Vol 215, Pt C.
9. Wyszynski, L. P., Aboagye, R., Stone, C. R., and Kalghatgi, G. T. (2004). 'Combustion Imaging and Analysis in a Gasoline Direct Injection Engine', SAE Technical Paper, No. 2004-01-0045.
10. Svensson, K. I., Mackrory, A. J., Richards, M. J. and Tree, D. R. (2005). 'Calibration of an RGB, CCD Camera and Interpretation of its Two-Color images for KL and Temperature', SAE Technical Paper, No. 2005-01-0648.
11. Touloukian, Y. S. and DeWitt, D. P. (1970). Thermal Radiative Properties --- Metallic Elements and Alloys, Thermophysical Properties of Matter Vol. 7, IFI/Plenum, New York-Washington.
12. Cignoli, F., De Iulii, S., Manta, V. and Zizak, G. (2001). 'Two-Dimensional Two-Wavelength Emission Technique for Soot Diagnostics', Applied Optics, Vol. 40, No. 30, pp. 5370-5378.
13. Murphy, J. J. and Shaddix, C. R. (2005). 'Influence of Scattering and Probe-Volume Heterogeneity on Soot Measurements Using Optical Pyrometry', Combustion and Flame, 143 1-10.
14. di Stasio, S., and Massoli, P. (1994). 'Influence of the Soot Property Uncertainties in Temperature and Volume-Fraction Measurements by Two-Color Pyrometry', Measurement Science and Technology, Vol. 5, No. 12, pp. 1453-1465.
15. Malvar, H. S., He, L. and Cutler, R. (2004). 'High-Quality Linear Interpolation for Demosaicing of Bayer-Patterned Color Images', Proceedings of IEEE ICASPP.
16. Weast, R. C. and Astle, M. J. (1981). CRC Handbook of Chemistry and Physics, CRC Press, Inc.

CONTACT

Hongrui.ma@eng.ox.ac.uk